Effect of Multi-scale Fractures on Oil Recovery from a Laminated Shale Reservoir

D. Leslie Zhang[1], Denis Klemin[2], Litao Shang[3], Zhiwei Wu[4], Jianquan Liu[3], Qingchuan Ye[3], Omar Reffell[5]*

[1]CNPCUSA Corp, Houston, TX, USA
[2]SLB, Houston, TX, USA
[3]CNPC Engineering Technology R&D Company Limited, Beijing, China
[4]China Petroleum Technical Service Corporation Limited, Beijing, China
[5]Core Laboratories LP, Houston, TX, USA

Abstract. Shale resources significantly enhance energy security through substantial unconventional oil and gas reserves accessed by technologies such as volumetric fracturing. Although field best practices to create complex fracture networks do exist, they lack fundamental research on how the scale of fractures affect recovery. Furthermore, understanding complex fluids and hydrodynamic processes in nano pore systems remain a key challenge to effective development of shale plays. The transport and production of oil and gas from the nano porosity matrix to the fractures are processes that are not well studied. This paper utilizes novel method of Density Functional Hydrodynamics to provide insights on how oil is produced from nano and micron sized matrix pores, helps to establish technical recovery limits as a function of rock texture, connects recovery analysis with the exact composition of reservoir fluids, study primary and secondary fractures to establish extends of stimulated reservoir volume and scale up this findings to the wellbore scale to provide field level insights. In this paper, sister plugs from a laminated shale oil reservoir in Dagang oilfield were acquired, with one being used to develop the characterization protocol and validate the digital rock model acquired on the sister plug, while the other being used to create digital rock models containing multi-scale fractures (primary, secondary, and micro) to study the contribution from fractures. Wellbore models containing primary and secondary fractures were created and recovery was simulated on the models with and without micro-fractures to assess their impact on each rock texture. It was shown that the contribution from low porosity bedding layers with higher clay content is minimal while both coarse- and fine-grained layers of high and medium porosity contribute the most towards production. Micro-fractures connect isolated pores and significantly increase oil production, especially in the first 4-6 months of production but can lead to a faster decline at latter stages of well life.

1 Introduction

Shale resources have emerged as a cornerstone of global energy production, significantly enhancing energy security through substantial unconventional oil and gas supplies. Multistage hydraulic fracturing is required to economically produce from unconventional reservoirs. Complex fracture networks are often desirable in unconventional reservoirs because they can increase stimulated reservoir volume and reservoir contact [1]. Studies [2-3] show that when natural and/or hydraulically induced micro-fractures are absent, only the near-frac regions in the Stimulated Reservoir Volume (SRV) are drained even for tight frac spacing. Oil remains trapped in the matrix between the principal frac zones. On the other hand, micro-fractures alone do not directly increase production unless connected to the hydraulic fractures [4-6]. Micro-fractures connected to the hydraulic fractures increase production rate and Estimated Ultimate Recovery (EUR) [4, 7-8]. The existing studies on the effect of multi-scale fractures on production are mostly based on fracture modelling. In this work, we constructed digital rock model to study the microscopic mechanisms of micro-fractures contribution to production.

Physical rock and fluid sampling and laboratory measurements are critically important to understand shale reservoirs [9]. Shale core analysis is challenging due to the complex mineralogical composition, laminated rock fabric, solid-fluid interfacial interactions, tight pore structure, presence of solid organic matter and residual fluid as well as fractures of multiple scales [10]. Here are some of the related challenges:

- Saturating shale samples are challenging and slow.
- No present mechanism to reliably check rock saturation (fully or partially saturated samples).
- Permeability, effective and total porosity measurements are challenging
- Any core flooding test is time consuming due to the tight pore structure and can take from month to years to complete. Establishing fluid-flow-dependent

* Corresponding author: Leslie.zhang@cnpcusa.com

measurements of capillary pressure and relative permeability is nearly impossible.

- Upscaling is challenging due to heterogeneity.

Digital rock technology can complement physical testing and provide important insights into understanding source rock reservoirs [11]. Studies of flow processes through nano sized constrictions require an account for additional physical phenomena [12] and further integration of each separate phenomena in a unified way [13]. This paper combines the most reliable shale rock lab techniques with digital rock analysis.

Core samples were collected from the second member of the Kongdian Formation (Kong-2 interval) in the Cangdong Sag. Within the Kong-2 interval, seven sweet layers have been identified. The present study focuses on the C3 layer within Kong-2 interval. This formation is characterized by substantial burial depth, elevated formation temperature, and high pressure. Lithologically, the Kong-2 interval is dominated by felsic, calcareous–dolomitic, and mixed shales, with an average clay content of approximately 16%, indicating relatively high rock brittleness. Well-developed lamination is observed in the Cangdong shale oil system, with felsic laminae exhibiting the highest oil content. The crude oil in this interval is characterized by high pour point, high wax content, and a low gas–oil ratio.

2 Methods

A whole core section from C3 was CT scanned. Two 1” diameter sister plugs were acquired next to each other containing the same beddings (Fig. 1). One sample was used for physical reservoir characterization study while the other was used to create digital rock models containing multi-scale fractures (primary, secondary, and micro) to study the contribution from fractures of different scale.

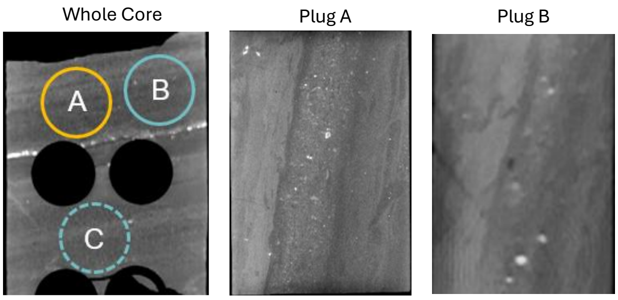

Fig. 1. Location of Plug A and B on the Whole Core Section. CT/microCT of the two plugs showing similar bedding planes. Plug A: microCT scanned at 25 micron/pixel resolution; Plug B: CT scanned at 250 micron/pixel resolution.

2.1 Shale Physical Characterization

Plug A was characterized for porosity, permeability, and pore size distribution using an integrated multi-disciplinary workflow (Fig. 2). The workflow mainly uses GRI crushed shale analysis and post cleaning HF NMR for porosity determination, which solved the problem of incomplete cleaning during GRI workflow; and uses HF NMR on as-receive samples prior to crushing to quantify fluid saturation, which solve the GRI problem of fluid loss during crushing. Ideally, porosity and saturation should be done on the same sample. But because Plug A was not long enough, GRI was done on a chunk taken from the same whole core section.

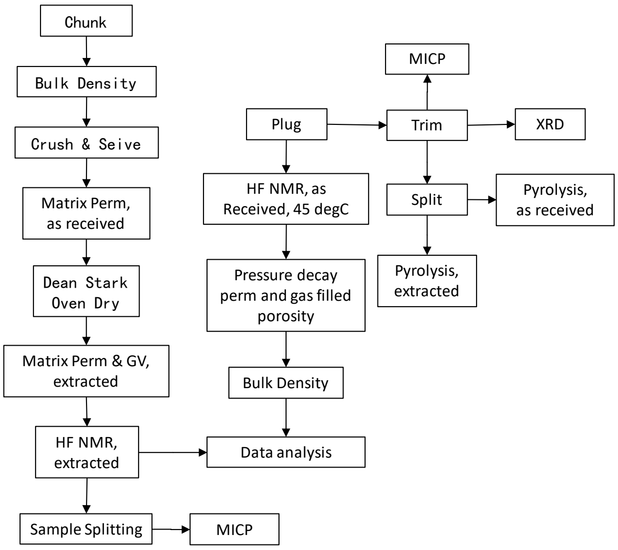

Fig. 2. Integrated Workflow to Characterize Shale

High-Frequency Nuclear Magnetic Resonance

Reffell et al [14] showed that when samples were crushed, fluid loss of both water and hydrocarbon happened. Therefore, the as-received NMR analysis was done on plug or chunks cut from whole core samples. Prior to as-received NMR analysis, the core piece was weighed, and an Archimedes bulk volume was measured using a non-wetting fluid. Bulk density was determined.

All NMR measurements were performed on a 23 MHz HF NMR spectrometer equipped with a probe that can accommodate core plug, chunks, or crushed materials. T2 data were acquired using the CPMG pulse sequence with an inter-echo spacing time of TE = 0.07 ms. T1 data were acquired using the inversion-recovery pulse sequence and the T1−T2 correlation. The T1-T2 map was obtained through a pulse sequence by combining T1 and T2 data acquisitions (61 T1 wait steps were used and 5000 echoes were recorded at each T1 wait step). The NMR signals were processed using an optimized truncated singular value decomposition (OTSVD) inversion method to obtain 1-D T1 or T2 distributions, and to construct the NMR T1−T2 maps [15].

HF NMR was performed on the as-received plug at 45 °C to increase the mobility of oil. 45 °C was chosen, with the addition of an applied pore pressure, to minimize the vaporization of the light and intermediate components in the oil. HF NMR was also done on the post cleaning GRI sample to quantify the residual fluids.

Pressure Decay Gas Permeability and Gas Filled Porosity

Gas permeability and gas-filled porosity was determined using the pressure decay method described in Gan et al. [16].

Plug A was placed in the sample cell of an SMP-200 instrument. Pressure of the reference cell was initially set around 200 psi. After opening the valve connecting the sample cell and reference cell, pressure immediately decreased to around 100 psi (depending on the void space volume) due to gas expansion. Pressure continued to decrease as gas diffused into the sample. Permeability was derived from the pressure decay profile. Grain volume was determined from the final equilibrium pressure, and gas filled porosity was calculated from the difference between the bulk volume and grain volume.

From the HF NMR water and oil filled porosity and pressure decay gas fill porosity measurements on Plug A, the total porosity can be quickly estimated.

GRI Crushed Shale Analysis

GRI crushed shale analysis was performed on a large chunk of core broken off from the same whole core section. The chunk was disaggregated to the standard GRI method 20/35 mesh size.

Crushed shale analysis not only reduces micro-fracture effects and shortens pore pathways, but also provides a uniform size and shape for permeability modelling. With the increased surface area, the pore systems could be accessed for more robust hydrocarbon cleaning and measured within a four-week period rather than months required for plug analysis.

Aliquot from each crushed sample was taken for as-received Rock-Eval pyrolysis. The remainder of the sample was immediately placed into pre-weighed dry thimbles and weighed for a total system weight. The samples were loaded into individual pre-conditioned Dean-Stark apparatus using Toluene and filled with Argon gas. Produced water volumes were recorded daily for seven days. The samples were unloaded and placed into a vacuum oven at 110 °C. The samples were dried until weight stabilized (+/- 0.01 g). Dry weight was recorded, and a grain volume was measured. NMR T1-T2 mapping was performed post-GRI drying.

Pyrolysis

Rock-Eval 6 was used in this study. Multi-heating rate (MHR) pyrolysis was done on as-received samples. A detailed description can be found in Carvajal-Ortiz et al. [17]. MHR program: Started at a temperature of 80°C, immediately ramped to 200°C at a rate of 50°C/minute, and maintained isothermal for 15 minutes. The second ramp of 50°C/minute to 250°C and maintained isothermal for 15 minutes. The third ramp of 50°C/minute to 300°C and maintained isothermal for 15 minutes. Fourth ramp of 50°C/minute to 350°C and maintained isothermal for 15 minutes. Fifth and last ramp of 25°C/minute to 650°C.

Mercury Injection Capillary Pressure

Mercury Injection Capillary Pressure (MICP) was done on the trims from the plug, and on the post cleaning crushed sample from the chunk. Samples are loaded into the glass penetrometers of the Micromeritics AutoPore mercury injection instrument. Ambient pore volumes and porosity were determined using helium derived grain volumes and toluene saturation data as a check against the Micromeritics determined values. A correlation permeability value was calculated from the mercury injection results using the Swanson method [18].

Apparent mercury injection volumes were corrected using a conformance factor determined for each sample from an evaluation of a plot of the apparent injection volume versus injection pressure.

2.2 Digital Core Analysis

2.2.1 Multi-Scale Imaging and Digital Rock and Fluid Model Construction

Plug A and B contain 3 distinct layers. The center layer is a mix of siltstone and mudstone, while the other two layers are mudstone. Due to the large variation in pore size and grain size, 6 resolution levels were required to fully characterize all three layers. The multi-scale imaging workflow is shown in Fig. 3.

Plug B was MicroCT scanned at resolution of 12 micron/pixel using Zeiss Xradia 520 Versa (level I). One end of the plug was polished then Argon milled using a Fischione Model 1060 SEM Argon Ion Mill to ensure a horizontal, flat, and polished surface optimal for high magnification SEM imaging. Overview SEM was done on a large area (3 by 14 mm) covering all 3 layers at resolution of 1 micron/pixel using Thermo Fisher Teneo FESEM (level III). The area was also analyzed for mineral identification and distribution using Advanced Mineral Identification and Characterization System (AMICS) and Bruker's QUANTAX energy dispersive X-ray spectrometry (EDS) system. A representative area in each of the three laminations were selected for medium resolution SEM at 200 nm/pixel and AMICS at 350 nm/pixel (level IV). The center of each medium SEM area was imaged at high resolution of 15 nm/pixel for Upper and bottom mudstone layers, and 25 nm/pixel for the center layer (level V). Areas with high nano porosity were selected for each layer for FIBSEM to analyze nano porosity and connectivity using FEI Helios NanoLab 660 (level VI). The center layer also has micro porosity, therefore miniplug was acquired and imaged at 1.566 micron/pixel using Zeiss Xradia 520 Versa microCT (level II).

FIBSEM images were segmented to extract pore space, then reconstructed to build high resolution digital rock models. Because the sample has high oil saturation, and the oil has high wax content and is solid at ambient conditions, the solid oil occupies many of the sample pores and block pore throats. Digital cleaning had to be done to all the images based on the oil to solid organics ratio identified by HF NMR and porosity values obtained on the sister plug A. MicroCT scans, SEM of various resolutions and high resolution models were processed and upscaled to build plug scale digital rock model.

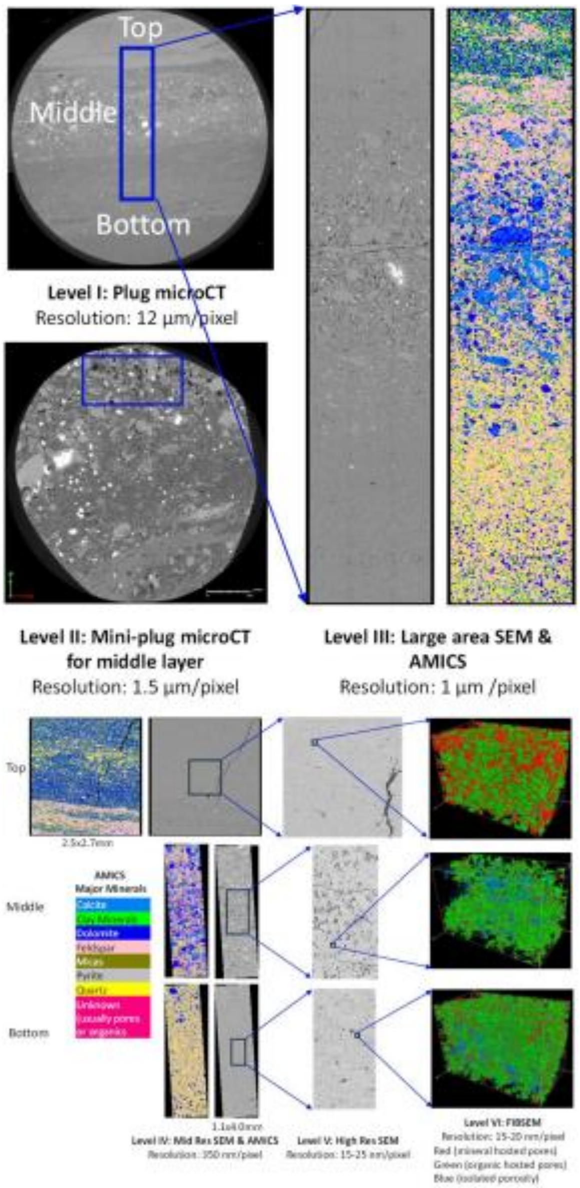

Fig. 3. Multi-Scale Imaging Workflow

Digital fluid models were built using the reservoir fluids PVT analysis data. Constructed fluid models considered reservoir temperature, range of pressures from initial reservoir pressure to the target end pressure, oil and brine phase properties as the function of pressure (viscosity, density, FVF, IFT), phase composition and phase envelope.

2.2.2 Simulation

Direct Hydrodynamic (DHD) flow simulator based on the density functional theory was used to model oil recovery in the laminated shale reservoir [19-21]. The DHD simulator is a numerical code that solves equations of the density functional hydrodynamics (DFH) [11, 22]. The equations are conservation laws for the mixture of chemical components, momentum, and energy with constitutive relations involving Helmholtz free energy or the entropy functional. These equations are used for description of multiphase compositional flows at the pore scale.

In DFH multicomponent mixture is defined via the integral parameters that characterize the mixture as a system of molecules. The primary variables are molar densities of chemical components, mass velocity of the medium, and internal energy density. DFH effectively combines thermodynamics and hydrodynamics of a multiphase multicomponent system via constitutive relations expressed as an entropy function in non-isothermal cases or by the Helmholtz energy function for isothermal problems.

Modeling accounts for complex wettability distribution across matrix pores of different types as well as primary and secondary fractures that accounts for presence of organic matter, prior pore saturation history obtained during the imaging phase, mineralogical data. Portions of rock surfaces in contact with oil at Swi conditions are generally rendered oil wet while clay hosted pores and surfaces of the pores saturated with water stay water wet, rendering samples mixed wet.

2.2.3 Upscaling

In the highest resolution models, it is assumed that the sub-resolution pores are effectively impermeable for oil at relevant oil/water capillary pressure levels. Direct simulation was conducted in resolvable pores. In lower resolution model, direct simulation was conducted in resolvable pore space while chemical potential drive method was utilized for sub-resolution pores [23]. The upscaled effective model considers chemical and multiphase transport, which makes it applicable to the same range of phenomena as DFH itself. The model's concept is that the transport is driven by gradients of chemical potentials of the chemical components in the fluid mixture and incorporate diffusion transport in addition to the pressure-driven transport.

3 Results and Discussion

3.1 Shale Physical Characterization

Plug A HF NMR at 45 ºC result can be found in Fig. 4. Region 1 – 4 are water, mobile oil, solid organics, and hydroxyls, as defined in Xie and Gan [10]. Excluding solid organics and bound water, HF NMR gives 1.3 p.u. water and 5.2 p.u. oil.

Pressure decay determined a total gas filled porosity of 1.2 p.u., among which, 0.02 p.u. comes from micro-fractures. This gives a total porosity estimate of 7.7% for plug A.

Residual fluid porosity on the chunk post GRI cleaning was also quantified by HF NMR. Combining with porosity determined on the GRI crushed sample, the porosity of the chunk was determined to be 7.8%. Porosity measured on plug A and the chunk are comparable.

As-received liquid phase saturation analysis shows that water saturation of plug A is 16% and oil saturation is ~67%. Table 1 compares hydrocarbon volume obtained by three different methods: GRI, HF NMR and MHR pyrolysis. The total hydrocarbon determined by HF NMR and MHR pyrolysis are comparable, but the quantity of producible oil from the two methods is very different. It shows that for heavy or waxy oil, even MHR pyrolysis underestimates the amount of producible oil because part of the producible oil does not volatilize at low temperatures and is instead thermally cracked during pyrolysis, contributing to S2 (thermally generated hydrocarbons) rather than S1 (free hydrocarbons). Therefore, estimating producible oil reserve and kerogen generating potential solely based on pyrolysis will be very far from reality.

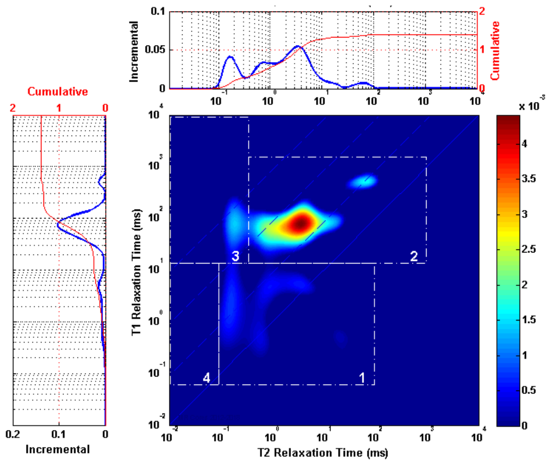

Fig. 4. Plug A HF NMR result

Table 1. Hydrocarbons Determined by Different Methods

GRI	HF NMR T1-T2			Pyrolysis		
Soluble HC	**Oil**	**Solid OM**	**Total HC**	**Oil (L1+L2+L3 +L4)**	**S2**	**Total HC**
mg/g	mg/g	mg/g	mg/g	mg/g	mg/g	mg/g
13.04	18.5	3.0	**21.4**	9.9	10.0	**19.9**

Mercury injection capillary pressure curve and the corresponding pore throat size distribution of plug A can be found in Fig. 5. Calculated Swanson permeability is 2.3 micro-Darcy, and median pore throat radius is 33 nm, indicating the dominance of the high perm streak in the middle of the sample. Because plug A contains nearly 70% solid oil, it was not possible to measure gas permeability on the plug.

3.2 Digital Rock Model Validation

Porosity of the high-resolution SEM (level V) images, FIBSEM models, and the medium resolution miniplug model for the center layer are compared in Table 2. The upscaled plug B model has a porosity of 6.5%, and permeability of 2.5 micro Darcy. Permeability compares well with plug A Swanson perm.

Mineral composition by AMICS for all three laminations is summarized in Table 3. Upper and center layers contain a significant amount of carbonate, while felsic dominates in the bottom shale layer. Clay content in the Upper layer shale is much higher than that of the bottom layer shale. Average felsic and carbonate content of plug B compares very well to the XRD results obtained on the trim of plug A.

Table 2. Digital Rock Model Properties

	Porosity, %			**Permeability, nD**	
Lamina	High Res SEM	FIBSEM	Mini-plug	FIBSEM	Mini-plug
Upper	4.32	4.68		5.84	
Center	10.45	5.36	10.74	78.2	2931
Bottom	6.46	8.42		116	

Table 3. Mineral Compositions

	AMICS Minerals（wt%）							
Lamina	Quartz	Feldspar	Felsic	Calcite	Dolomite	Carbonate	Pyrite	Clay + Mica
Upper	8.3	36.1	44.4	9.4	30.6	40.0	0.1	15.4
Center	7.1	43.7	50.8	21.7	20.3	42.0	3.1	4.1
Bottom	20.1	58.2	78.3	4.2	10.5	14.6	0.3	6.8
Average	11.8	46.0	57.8	11.8	20.4	32.2	1.2	8.8
XRD	14.8	41.4	56.2	10.3	21.9	32.2	1.7	9.9

Note: Felsic is a group combining quartz and feldspar

Digital mercury injection was simulated on small models and upscaled to the plug B model. Capillary pressure and pore throat radius were compared to the measured data on plug A in Figure 5 and shows good agreement.

3.3 Effect of Multi-Scale Fractures on Oil Recovery

3.3.1 Micro-Scale

High-resolution models based on FIBSEM scans are 12-30 micron in any of the three dimensions. Studying the effect of fractures at micro-scale helps to identify the effect of different scales of fractures.

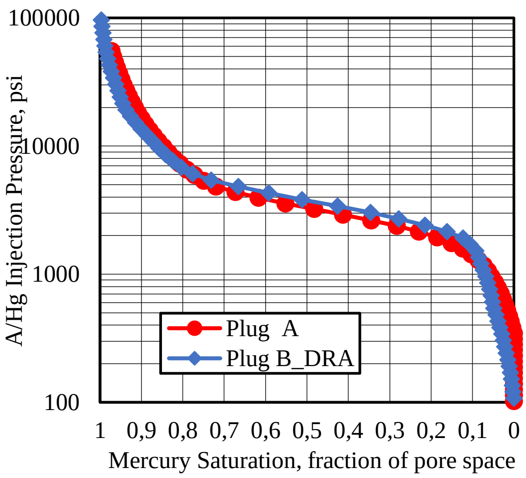

(a) Mercury injection capillary pressure

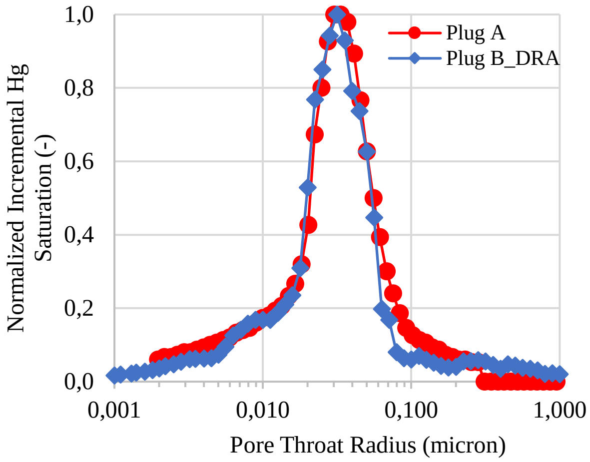

(b) Pore Throat Size Distribution

Fig. 5. Comparison of Plug A Mercury Injection Test Results and Plug B Simulated Mercury Injection on the Upscaled Digital Rock Model

From plug microCT, it was observed that most micro-fractures are parallel to bedding, except in the Upper layer, where micro-fractures normal to bedding also exist. Therefore, in the high-resolution model for the Upper lamina, a micro-fracture normal to bedding and a micro-fracture parallel to bedding were introduced; two micro-fracture parallel to bedding were inserted into the high-resolution models for the center and bottom layers. All micro-fracture width is 0.5 micron at this scale.

Connate water saturation was established by simulating oil displacing water in the models with and without micro-fractures. Results for the Upper layer are shown in Fig. 6. Porosity of the Upper layer is the lowest among the three and pores are poorly connected. Without micro-fractures it has a high initial water saturation of 31.46%. Micro-fractures greatly improve the pore connectivity for the Upper layer and reduce initial water saturation to 14.53%. Similarly, micro-fractures also improve connectivity in the center and bottom layers and reduce initial water saturation of center layer from 22.61% to 9.44%, and of bottom layer from 18.97% to 17.15%. The bottom lamina has the best connectivity and improvement from micro-factures is small. The average water saturation of the three laminae is 24.35%, close to the field value of 23.5%.

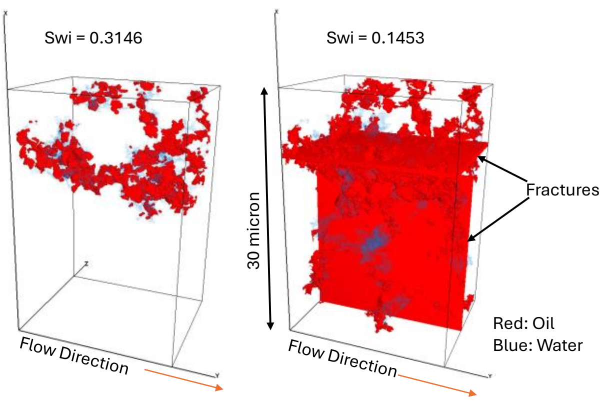

Fig. 6. Micro-Fractures Improve Connectivity of Nano-Porosity in the Upper Lamina

Oil recovery by depletion was simulated on the high-resolution models with and without micro-fractures in 3 phase formulation (oil, gas and water). Production is from 1 of the 6 faces, assuming hydraulic fracture is on that face. During oil depletion, when the pressure is above the bubble-point pressure, oil production is driven by oil compressibility; when pressure reaches the bubble-point pressure, gas expands and displaces oil. As oil is produced, gas continues to expand and occupy the pore space vacated by the produced oil. As gas is produced, the composition of the remaining oil continues to change, so the GOR of the remaining oil differs from the initial GOR. When the gas and liquid phases become completely separated, oil production stops [19]. Portion of the mobile water is produced while the bound water stays in pores.

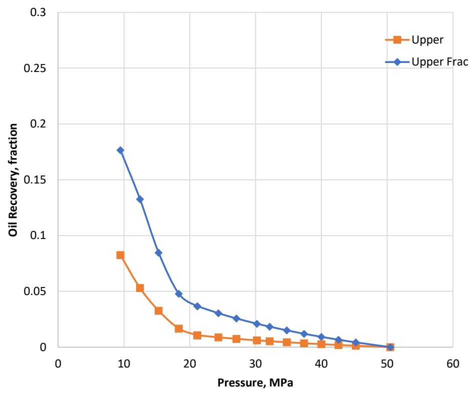

(a) Upper

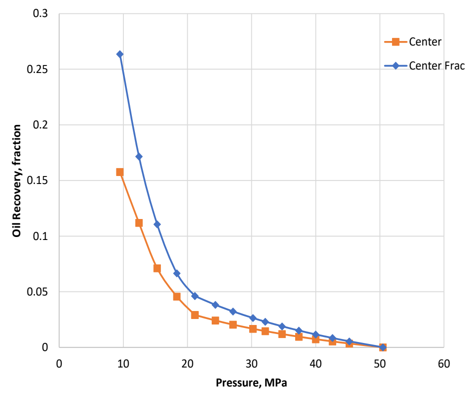

(b) Center

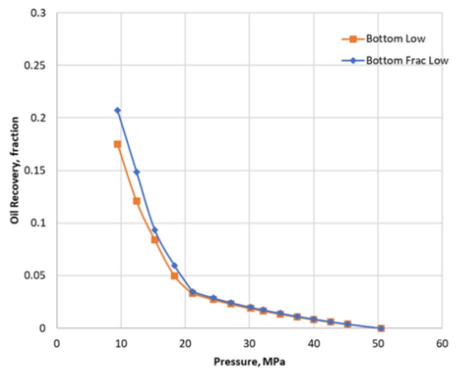

(c) Bottom

Fig. 7. Micro-Fractures Improve Oil Recovery Differently for the Three Laminae

Results are shown in Fig. 7, with orange curves for the case without micro-fractures and blue curves for the case with micro-fractures. Micro-fractures improve recovery by increasing pore connectivity, therefore the poorly connected Upper layer saw the greatest improvement and the well-connected bottom layer saw the least improvement.

Results of medium resolution model based on the center layer microCT are similar to that of the high-resolution model and will be skipped here.

3.3.2 Plug-Scale

All 6 levels of imaging were utilized to build the upscaled plug model. A square prism with horizontal bedding was cut from the plug model for simulation. Naturally occurring micro-fractures were removed from the model. Primary and secondary fractures were introduced into the model normal to bedding and to each other, see Fig. 8. Primary fracture width is 40 mesh (400 micron) and secondary fracture width is 105 mesh (142 micron). Micro-fractures parallel and normal to beddings were also introduced into the plug model to study the effects of microfractures (Fig. 8 (c)). Micro-fractures are only connected to other microfractures or secondary fracture. The boundary between microfractures and primary fracture is impermeable.

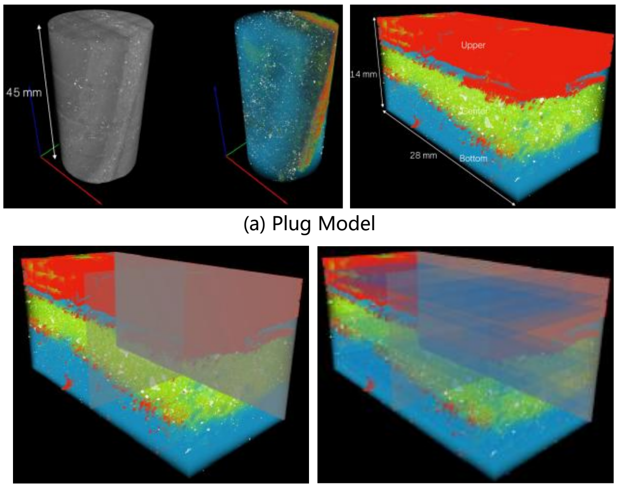

(a) Plug Model

(b) Plug Model with Primary and Secondary Fractures

(c) Plug Model with Primary, Secondary, and Micro-Fractures

Fig. 8. Upscaled Plug Model with or Without Primary, Secondary, and Micro-Fractures

Results of oil recovery by primary depletion with and without micro-fractures can be found in Fig. 9. Primary and secondary fractures can ultimately recover 14.5% oil, while the addition of micro-fractures can add another 7%, which is close to an increase of 50% of the no-micro-fracture case.

3.3.3 Well-Scale

To access the production rate of each rock type at large scale, wellbore model was created that contain a horizontal well of 1840 meter long, containing 80 frac stages. Wellbore model was populated with each of the data from three high resolution models, and the medium resolution model for the center layer. This includes oil, gas and brine phase transport properties as a function of saturation and pore pressure, porosity, saturation data obtained on the high resolution models, primary and secondary fracture density and dimensions and conductivity established using proppant embedment laboratory testing data. The production rate with and without micro-fractures can be found in Fig. 10. It is shown that the upper layer contributes little to production if only primary fractures are present. When micro-fractures are also present, the initial production rate increased almost 20 times, but production declines rapidly. In contrast, the bottom shale layer is of much better reservoir quality and has much higher production rate and the decline is gradual. When micro-fractures are present, production rate more than doubles than without. Without micro-fractures, the center lamina has similar production rate as the bottom shale layer. With micro-fractures, production rate of the center lamina is much higher due to higher permeability and porosity.

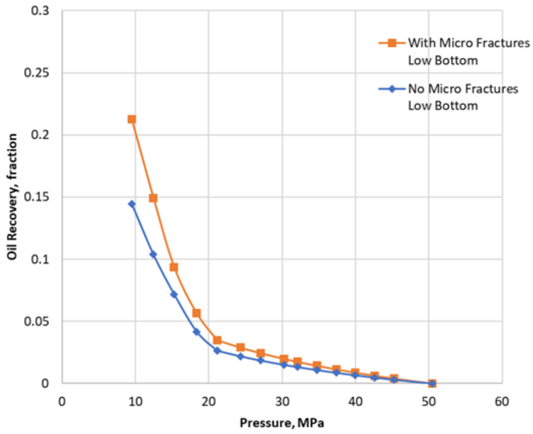

Fig. 9. Comparison of Oil Recovery with and without Micro-Fractures at the Plug Scale

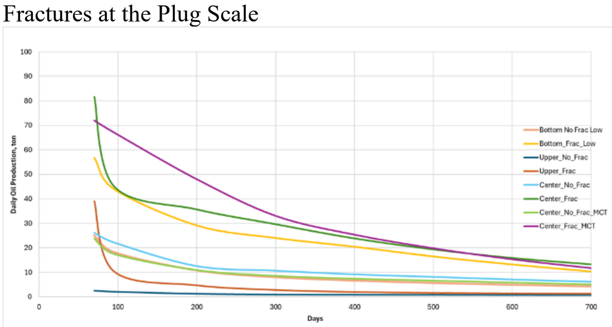

Fig. 10. Comparison of Oil Recovery with and without Micro-Fractures at Well Scale

4 Conclusions

This work describes steps taken to construct digital rock models of laminated rocks observed in the Cangdong shale oil system. Constructed models were validated using laboratory core analysis data for porosity, permeability, pore throat size distribution, initial saturation. Once validated, microscopic mechanisms of micro-fracture contribution to production were studied on the constructed digital rock models. It was demonstrated that during oil depletion, when the pressure is above the bubble-point pressure, oil production is driven by oil compressibility; when pressure reaches the bubble-point pressure, gas expands and displaces oil. As oil is produced, gas continues to expand and occupy the pore space vacated by the produced oil. It was demonstrated that micro-fractures improve recovery by increasing pore connectivity, therefore the poorly connected Upper layer saw the greatest improvement and the well-connected bottom layer saw the least improvement. Plug level modeling data allowed to account and impact of combined presence of primary and secondary fractures on oil recovery. Primary and secondary fractures can help to ultimately recover 14.5% oil, while the addition of micro-fractures can add another 7%, which is close to an increase of 50% of the no-micro-fracture case. Wellbore models helped to assess the production potential of each layer studied and establish connection between pore scale recovery efficacy and well production.

In summary:

1. Plug A was characterized using a protocol that integrated HF NMR, GRI, pyrolysis, XRD, and MICP. The plug was found to have a porosity of 7.8%, permeability of 2.3 mD, and median pore throat radius of 33 nm.
2. Plug B was characterized using multi-scale imaging of 6 levels. Permeability, pore throat size distribution and mineral content matched those of the sister plug very well. Porosity is off by 1%, which could be due to more upper layer in plug B than plug A.
3. Micro-scale simulation shows that micro-fractures increase oil production by increasing pore connectivity.
4. Wellbore modelling showed that the contribution from low porosity bedding layer with higher clay content is minimal while both coarse- and fine-grained layers of high and medium porosity contribute the most towards production.
5. Micro-fractures connect isolated pores and significantly increase oil production, especially in the first 4-6 months of production but can lead to a faster decline at latter stages of well life.

Acknowledgments

Authors thank CNPC and SLB for permission to publish this work, Ritesh Bhakta for his assistance throughout this project.

References

1. M.J. Mayerhofer, E.P. Lolon, N.R. Warpinski, C.L. Cipolla, D. Walser, C.M. Rightmire, SPE Prod & Oper **25 (01)**, 89 (2010)
2. R. Weijermars, A. van Harmelen, L. Zuo, URTEC-2670073B (2017)
3. G. Fuentes-Cruz, P.P. Valkó, SPE J. **20 (01)**, 124 (2015)
4. O.G. Apaydin, E. Ozkan, R.S. Raghavan, SPE Res Eval & Eng **15 (04)**, 473 (2012)
5. A. Khanal, R. Weijermars, Pet. Sci. **16**, 550 (2019)
6. S. Apiwathanasorn, C. Ehlig-Economides, SPE-162842-MS (2012)
7. W. Yu, X. Hu, M. Liu, W. Wang, Energies **12 (5)**, 932 (2019)
8. C. Chang, Y. Li, X. Li, C. Liu, M. Fiallos-Torres, W. Yu, Energies **13 (11)**, 2853 (2020)
9. Y. Wang, Z. Wang, Z. Zhang, S. Yao, H. Zhang, G. Zheng, F. Luo, L. Feng, K. Liu, L. Jiang, Energy Reviews, **3 (2)**, 100067 (2024)
10. M. Ostadhassan, K. Liu, C. Li , S. Khatibi, *Fine Scale Characterization of Shale Reservoirs: Methods and Challenges* (Springer, 2018)
11. A.Y. Demianov, O.Y..Dinariev, N.V. Evseev, *Introduction to the density functional method in hydrodynamics* (Moscow, Fizmatlit, 2014)
12. B. Bhushan, (Ed.), *Springer Handbook on Nanotechnology* (Berlin, Springer-Verlag, 2004)
13. O.Y. Dinariev, and N.V. Evseev, Phys. Rev. E, **95,** 063307 (2017)
14. O. Reffell, Z.H. Xie, H. Carvajal-Ortiz, SPWLA-2022-0083 (2022)
15. Z.H. Xie, Z. Gan, SPWLA-2018-FFFF (2018)
16. Z. Gan, T. Griffin, J. Dacy, H. Xie, R. Lee, SPWLA-2018-DD (2018)
17. H. Carvajal-Ortiz, T. Gentzis, H. Xie, URTeC-2019-1005 (2019)
18. B.F. Swanson, J. Pet. Technol. **33 (12)**, 2498 (1981)
19. S.I. Geetan, R.M. MacDonald, D. Klemin, URTeC - 2016-2461115 (2016)
20. S.I. Geetan, R.M. MacDonald, D. Klemin, URTeC - 2017-2671283 (2017)
21. R.M. MacDonald, S.I. Geetan, D. Klemin, URTeC - 2018- 2902911 (2018)
22. A.Y. Demianov, O.Y. Dinariev, N.V. Evseev, Can. J. Chem. Eng. **89**, 206 (2011)
23. O. Dinariev, N. Evseev, D. Klemin, SCA2019-002 (2019)